https://www.scirp.org/journal/ns Natural Science, 2026, Vol. 18, (No. 7), pp: 158-180

Statistical and Spectral Analysis of the Carbon Dioxide Variations in Terrestrial Environment

Valentina V. Zharkova[1,2], **Irina Vasilieva**[2,3]

[1]Department of MPEE, Faculty of Engineering and Environment, University of Northumbria, Newcastle upon Tyne, UK; [2]ZVS Research Enterprise Ltd., London, UK; [3]Department of Solar Physics, Main Astronomical Observatory, Kyiv, Ukraine

Correspondence to: Valentina V. Zharkova, valentina.zharkova@northumbria.ac.uk;
Irina Vasilieva, valja46@gmail.com

Keywords: Sun: Magnetic Field, Earth: Temperature, Earth: Sea Level, Earth: Carbon Dioxide, Wavelet Analysis
Received: May 25, 2026 **Accepted:** July 20, 2026 **Published:** July 23, 2026

ABSTRACT

We analyse annual mean and annual growth rate measurements of the global CO_2 abundances taken from the NOAA General Monitoring Laboratory (GML). The annual CO_2 variations are shown to be best described by a parabolic fit with concavity up, in contrast to a linear trend often attributed to fossil-fuel emissions. Global CO_2 abundance variations were shown to correlate (r = 0.60) with variations of the Global Mean Sea Level (GMSL), Oceanic Nina Index/El Nino Southern Oscillations (ONI/ENSO) (r = 0.24) and global terrestrial temperature (r = 0.82). De-trended CO_2 variations show much stronger correlation with ONI/ENSO (r = 0.79). Morlet wavelet spectral analysis of CO_2 abundances reveals significant periods of 21.4, 9, and 3.7 years. Similar periods appear in GMSL (21.4 and 8.5 years), ONI/ENSO (21.4, shared 21.4-year period indicates influence from cyclic variations in solar magnetic activity (double solar cycle). The 9-year CO_2 oscillation, together with the strong correlation of detrended CO_2 with ONI/ENSO, links to ENSO variations spanning 4.5 - 12 years. The spectral analysis with Morlet's wavelet of the variations of CO_2 abundances reveals the natural periods of 21.4, 9 and 3.7 years. The similar periods are derived for the variations of GMSL (21.4, and 8.5 years), ONI/ENSO index (21.4, 12 and 4.5 years) and the GLB terrestrial temperature (21.4, 8.36 and 3.75 years). The presence of a common period of 21.4 years indicates that all the datasets are affected by cyclic variations of the solar magnetic activity in a double solar cycle. The measured CO_2 oscillations with a period of 9 years combined with the correlation of the de-trended CO_2 abundances can be linked to the ONI/ENSO variations ranging within the periods of 4.5 and 12 years. Cross-correlation analysis shows a time lag of approximately one year in variations of the global CO_2 abundance relative to the global terrestrial temperature. Wavelet coherence

analysis confirms a time lag of 1.2 - 1.8 years for the global CO_2 abundance to fall behind the temperature during most temporal intervals. These results indicate that global CO_2 variations follow temperature variations rather than driving them.

1. INTRODUCTION

The carbon dioxide (CO_2) abundance variations are often linked to the variations of terrestrial temperature and sea level variations. Furthermore, here is a 50% increase in vegetation productivity since 1900 can be attributed to higher atmospheric CO_2 concentrations and a longer growing season.

Keeling *et al.* [1] documented a steady rise in CO_2 abundances since 1985, which has been widely cited as evidence for anthropogenic influence of CO_2 during the industrial era. This interpretation has been challenged on methodological grounds [2, 3], who claimed that the errors in these revised values were of a similar magnitude to the apparent increase in the atmospheric CO_2 level imposed by the wrong assumptions such as: no liquid phase in polar ice; younger age of air than of ice due to free gas exchange between deep firn and the atmosphere; and no change in composition of air inclusions [2].

Using two-dimensional regression analysis Ahlbeck [4] shown that the airborne fraction of CO_2 emissions has declined despite ongoing warming, suggesting enhanced sinks in the biosphere and oceans. Soares [5] reported that temperature changes generally precede CO_2 changes across diverse conditions. The author indicated that unlike CO_2 abundance, the water vapour in the atmosphere is rising in tune with temperature changes, even on a monthly scale [5].

Salby and Harde [6] noted a strong temperature dependence on the seawater CO_2 partial pressure. Veyres *et al.* [7] found no correlation between detrended 12-month CO_2 increments and fossil-fuel emissions, estimating that only 5.5% of atmospheric CO_2 originates from the unabsorbed fossil-fuel sources while 94.5% originates from natural outgassing of oceans and soils. This interpretation is supported by the $\delta^{13}C$ records at Mauna Loa Observatory (MLO) and other research [8] showing that the standard metric of $\delta^{13}C$ is consistent with an input isotopic signature being stable over the entire period of observations (>40 years) not affected by the increases in human CO_2 emissions.

The average CO_2 increase in the atmosphere, measured accurately by infrared spectrometry at Mauna Loa (NOAA, 2015), is 1.99 part per million (ppm) per year from 1995 to 2014 [9]. The largest yearly increase observed in 1998, nearly 3 ppm, followed the largest El Niño warm fluctuation by 10 months. Other CO_2 increases above the mean such as 2.52 ppm in 2005, 2.42 ppm in 2010, 2.65 ppm in 2012 or 2.28 ppm in 2014, also follow by 9 - 11 months [10]. El Niño temperature fluctuations parameterised via the Multivariate ENSO (El Niño Southern Oscillation) index (MEI, 2014). ARIMA time-series modelling further supports the correlation between 12-month increments of MLO CO_2 and SST [9].

The other studies by different authors (see, for example [8, 11-13]) addressed the role of natural factors (the sun and volcanic eruptions) comparing to that from CO_2 led linear anthropogenic contributions. Roy [11] identifies that dominance of Central Pacific (CP) Ocean Nino Index (ONI) or El Nino Southern Oscillation ENSO) and associated water vapour feedback during that period plays an important role in the formation of CO_2 variations that confirms the suggestions its natural cause [12].

In addition, Ato [14] reported that the ocean temperatures and not human-made carbon dioxide emissions, are the primary drivers of the atmospheric CO_2 changes confirmed by other research [4, 6]. Furthermore, Koutsoyiannis *et al.* [15] have shown that the causal relationship between an increase of the terrestrial temperature and a growth of the CO_2 abundances clearly indicates that the CO_2 presence must be a consequence of the terrestrial temperature growth and not its reason as assumed by the modern temperature models [16]. Hence, the causal direction between the variations of temperature and CO_2 abundances remains debated.

The present study performs statistical and spectral analyses of observational terrestrial datasets to identify robust links between CO_2 abundances and key terrestrial parameters (temperature, sea level, and ONI/ENSO) index, with particular attention to periodicities and lead-lag relationships.

2. DESCRIPTION OF THE TERRESTRIAL ENVIRONMENT DATA

2.1. Observations of Carbon Dioxide Annual and Growth Variations

For the variations of carbon dioxide, we analysed publicly available, long-term observational datasets selected for global or near-global coverage, multi-decadal length, and standardised protocols provided by the NOAA's Global Monitoring Laboratory (GML), which measures the abundances of carbon dioxide and other greenhouse gasses in the air [17, 18]. Carbon dioxide data (ppm, dry-air mole fraction) were obtained from NOAA GML: globally averaged marine surface annual means and annual growth rates [17]-[19]. These are derived from the CO_2 data obtained by the worldwide station network (including Mauna Loa and American Samoa) using Monte Carlo averaging [19].

We use two CO_2 datasets: 1) globally averaged marine surface CO_2 annual mean data: https://gml.noaa.gov/ccgg/trends/gl_data.html; https://gml.noaa.gov/webdata/ccgg/trends/co2/co2_annmean_gl.txt and 2) globally averaged marine surface annual mean CO_2 growth rates: https://gml.noaa.gov/ccgg/trends/data.html; https://gml.noaa.gov/webdata/ccgg/trends/co2/co2_gr_gl.txt. The annual mean (averaged) CO_2 data is shown in **Figure 1** and the growth rate CO_2 data variations are presented in **Figure 2**.

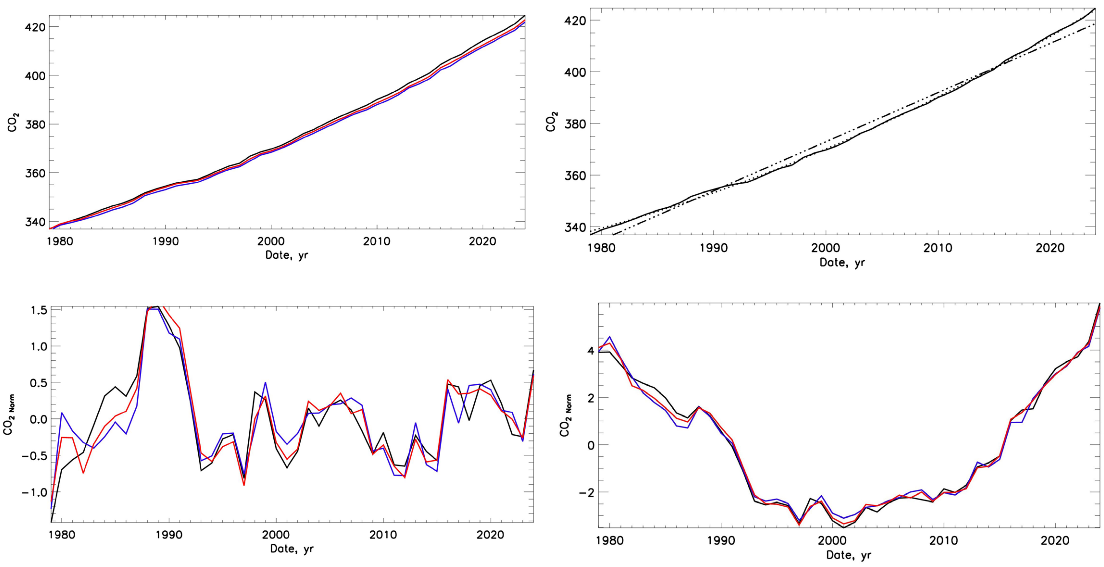

Figure 1. Top plot: the annual variations of CO_2 abundances (solid curve) observed in Samoa (blue curve), MLO (black curve) and global (red curve) (left) and approximation of global CO_2 abundances (solid curve) by a linear approximation (dot-dashed curve) (right). Bottom plot: the deviations of CO_2 abundances from their parabolic (left) and linear (right) approximations.

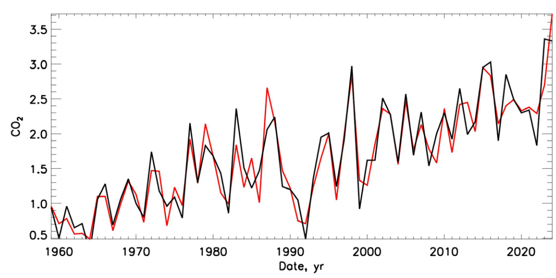

Figure 2. The variations of CO_2 abundances (growth rate) measured by the MLO (black curve) and derived from all the stations, as global CO_2 variations (red curve).

The key points of CO_2 measurements include the following locations: Barrow, Alaska (BA); Mauna Loa Observatory (MLO), Hawaii; American Samoa (Samoa) and Southern pole (SP), Antarctica. Since 1973 the GML secures the uninterrupted measurements of the carbon dioxide abundances [17] that allows one to derive a high level of details in the seasonal, short-term and long-term variations of these carbon dioxide abundances. The series of the MLO observations in the northern subtropics is obtained at the height of 3400 m above sea level provide the longest observations of carbon dioxide abundances started in March 1958 by C. David Keeling [1]. Because of its height of 3400 m above the sea level, the MLO data have some understandable systematic differences from the other data measured close to the surface at the sea level.

The annual variations of CO_2 abundances measured by Samoa, MLO and global data are shown in **Figure 1** revealing that global variations reflect very closely the CO_2 variations measured by Samoa or MLO sites. The polynomial approximation of the observed global CO_2 variations (solid curve) was conducted by a linear (dash-dotted curve) (**Figure 1**, top right plot) and parabolic (quadratic) line fitting closely the observed curves (dark and red lines) shown in **Figure 1**, top left plot). The deviations of the measured global CO_2 curve from the polynomial approximations are shown in **Figure 1**, bottom plots for parabolic (left) and linear (right) fits.

It can be seen that the linear polynomial fit of the averaged annual CO_2 variations observed between 1990 and 2015 reveals a systematic deviation of the linear curve (dash-dotted line) from the observed one (solid line) (**Figure 1**, bottom right plot). While the parabolic (quadratic) polynomial fit (**Figure 1**, bottom left plot) shows very small randomly distributed differences between real and parabolic curves reflecting a good approximation.

These differences in the deviations of the real CO_2 averaged annual curve and polynomial fits indicate that the measured global CO_2 variations are best described as a positive parabolic function with a concavity up (the parabola opens upwards) and not by a linear curve assigned by IPCC to the increase of CO_2 from a usage of fossil fuel. In the other words, the residual analysis showed systematic, non-random deviations for linear fits (1990-2015) but a random scatter for the parabolic fit, supporting an upward-opening parabolic description of the observed temporal CO_2 variations.

This means that the measurements of the total (global) CO_2 variations, which by default should include both natural and human-induced CO_2 abundances, do not reveal any noticeable similarity of the measured $C)_2$ curve to the linear CO_2 abundances produced by the fossil fuel usage. This conclusion is also supported by the lack of increase of the carbon isotope ^{13}C in the past 40 years usually produced by fossil fuels [8].

The examples of real (not annually averaged) trends in the CO_2 abundance variations measured by MLO and global data are presented in **Figure 2**. This comparison show pretty close correspondence of both the datasets while revealing noticeable temporal fluctuations of the real CO_2 abundance data. These measured CO_2 variations can be explored for comparison with the other terrestrial data as discussed in section 2.2 and used for the wavelet spectral analysis described in section 3.

2.2. Observations of Temperature, Sea Level and Ocean Nina Index (ONI)

2.2.1. The Terrestrial Temperature Variations

In this research we consider the two series of terrestrial temperature measurements, which have a global coverage of the terrestrial regions not affected by any local phenomena, like El Nino/La NIna events in the Pacific ocean area. The first set is developed by the British Meteorological Center in Hadley and the department of Climate Research of the East Anglia University https://www.metoffice.gov.uk/hadobs/hadcrut5/ [20], accessed on 12/06/2023. This series is named as HADCRUT5 for the future reference. The second set called GLB hereafter, is the series of the surface temperature (GISSTEMP) produced by the NASA Goddard Institute of Space Science (GISS) https://data.giss.nasa.gov/gistemp/tabledata_v4/GLB.Ts+dSST.txt accessed 12/06/2023 [21].

The both sets are shown in **Figure 3** in the top plot for the HADCRUT5 set (red curve) and GLB set (black curve) and in the bottom plot there is a difference of these two datasets is presented. It can be seen that the two temperature datasets are rather close besides in the interval of 1880-1910 when GLB set has systematically higher magnitudes. The difference between these two series seems to be not so large as shown in **Figure 3**. Although it leads to some noticeable discrepancies revealed during the analysis of the periodic part of the series discussed below. In order to exclude the effects of limited lengths of the series, for a comparison with CO_2 variations we will use the GLB data. The GLB temperature variations will be compared with the variations of CO_2 abundances in section 4.2.3.

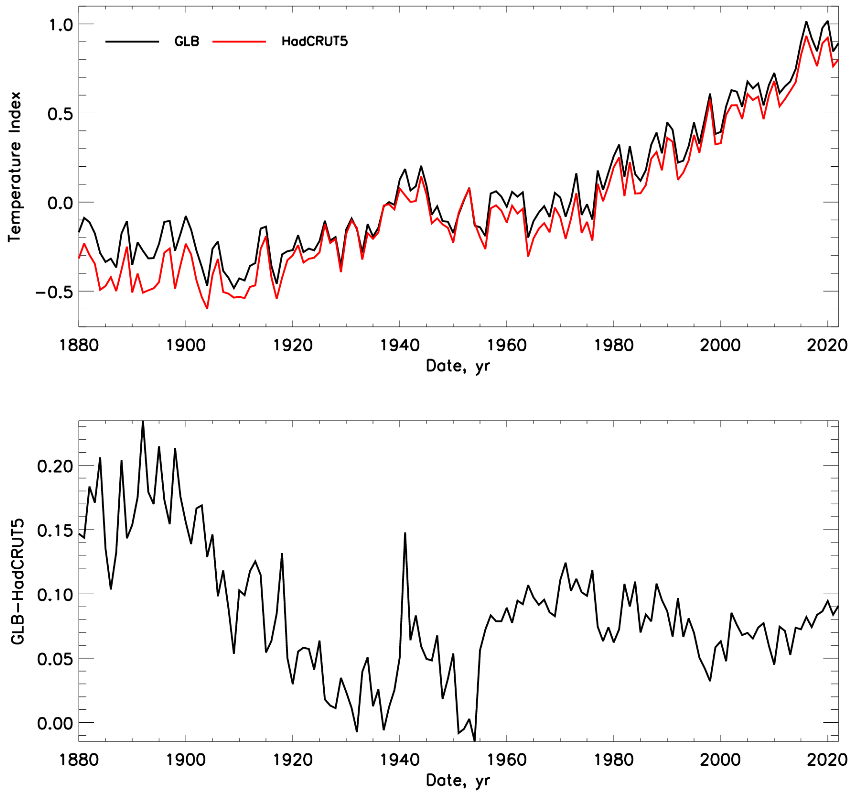

Figure 3. Top plot: the series of terrestrial temperature variations HADCRUT5 (red curve) and GLB (black curve). Bottom plot: the difference between GLB and HadCRUT5 data.

2.2.2. The Sea Level Variations

The series of temporal variations of the Global Mean Sea Level (GMSL) during 1880-2014 (named as GMSL (2015)) was obtained from the Centre for Protection of the Environment of the USA and SCIRO (Centre for Scientific and Industrial Research Organisation) (http://www.cmar.csiro.au/sealevel/sl_data_cmar.html accessed on 29/07/2023 [22]).

The GLB temperature (black curve) and its approximation by the 4th degree polynomial (red curve) is shown in **Figure 4** (top left plot) with real GMSL measurements (black line) and the averaged one by the 4th-order polynomial (red line) are shown in **Figure 4** (top right plot). In **Figure 4**, bottom left plot there are the de-trended GMSL sea level variations (black curve) calculated by subtracting from the data defined by the averaged data shown in **Figure 4**, top right plot, versus the GLB temperature (blue plot) and the summary curve of the solar magnetic activity (red curve) [23].

The GMSL data were checked against a 2019 extension (named GMSL 2019) for robustness. In **Figure 4**, bottom right plot there is comparison of the GMSL 2019 with the GMSL data GMSL 2015) which was used in our previous research [24]. The GMSL data for 2019 were corrected by the increased normalisation by 128 mm combined with strong variations of the measurements after 1990. To avoid these fluctuations, in the current paper we mainly used the first (uncorrected) dataset of GMSL 2015 as there were no explanation provided by the site for the corrections in the set GMSL 2019.

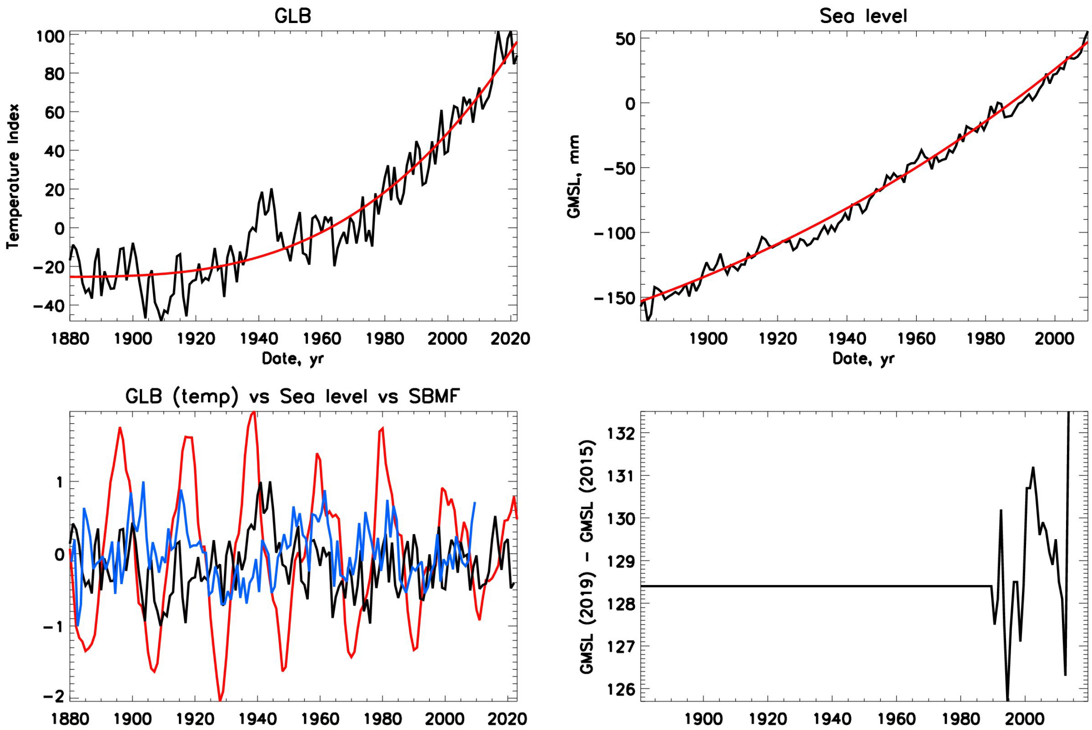

Figure 4. Top plot left: the variation of global GLB temperature (black curve) and approximation by a polynomial of 4th degree (red curve), Top plot right: the global mean sea level (GMSL) variations for 1870-2014 (black curve) and averaged curve presented by a polynomial of the 4th degree (red curve). Bottom left plot: comparison of the GLB temperature variations (black curve) with the de-trended sea level variations (blue curve) calculated by subtracting the averaged sea level from the real sea level curve. The red curve represents the summary curve of solar background magnetic field defining the magnetic solar cycle of 21.4 years [23]. Bottom right plot: a comparison of the two temporal versions of GMSL releases in 2015 and 2019 with renormalisation by 128 mm in 2019 and introduction of some unrecognised measurements from 1990 onwards.

It can be observed that the sea level was increasing from 1870 until 2004 with an averaged speed of growth of 1.7 ± 0.3 mm/year [25], or of 3.1 ± 0.7 mm/y ([26, 27]. Although during the period of 1971-2018 and 3.7 (3.2 - 4.2) during the period of 2006-2018, the average growth speed of 2.3 ranged from 1.6 to 3.1 mm/y [28].

This increase of the GMSL sea level show, in average, a close similarity to the temporal variations of the GLB temperature curve reported in the previous studies [24, 29-34]. Furthermore, the de-trended fluctuations of the GMSL sea level (blue curve) shown in **Figure 4**, bottom left plot, follow closely the GLB temperature variations (black curve). In addition, these GMSL and GLB variations reveal some links with the solar magnetic activity with a period of 21.4 years (red curve) as it was noted earlier [24]. The GMSL variations will be compared with the variations of CO_2 abundances in section 4.2.1.

2.2.3. The Oceanic Nina Index, or El Nina Southern Oscillations (ONI/ENSO)

The Oceanic Nina Index (ONI,) which also called as El Nino Southern Oscillation (ENSO), e.g. the ONI 3.4 index, is available since 1854 from the site https://www.climate.gov/news-features/understanding-climate/climate-variability-oceanic-nino-index [35]. The ONI index follows the three months measurements of an average temperature of the sea surface in the East-Central tropical part of the Pacific ocean nearby the international line of the date change above the averaged one over 30 years.

The temporal variations of the ONI/ENSO index from 1950 till present is shown in Figure 5, bottom plot, where the red colour shows the excesses above the averaged ENSO index and the blue colour shows the reductions below the averaged index. Figure 5 shows the temporal variations of the Global Land-Ocean Temperature (GLB) Index (black curve) [21] versus variations of ONI/ENSO Index (multi-coloured curve).

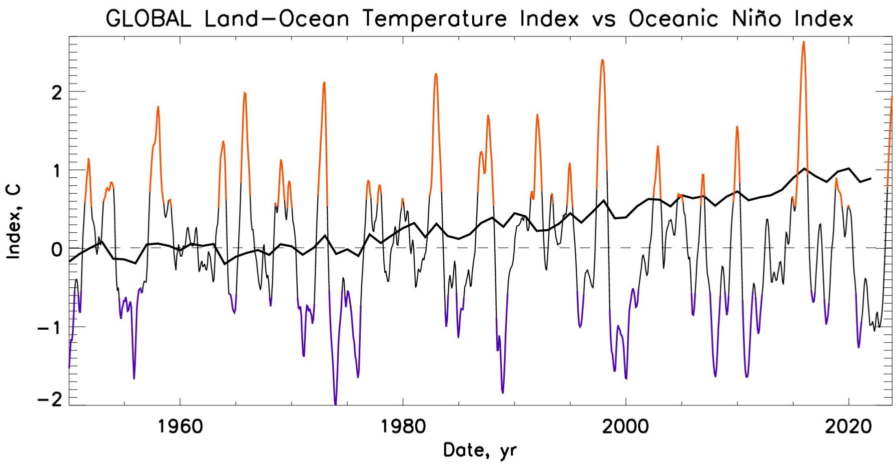

Figure 5. Temporal variations of the combined land-surface air and sea-surface temperature, GLOT (black curve) and of the Oceanic Nina Index (ONI), or El Nina Southern Oscillation (ENSO) index (multi-coloured curve). The red colour shows the excesses (hot periods) above the averaged ONI/ENSO index and purple colour shows the reductions (cold periods) below the averaged ONI/ENSO index.

From a comparison of the curves tone can observe that there is a strong visible link between the ONI/ENSO index and the increase of the global land-ocean (GLB) temperature. The scatter plot of correlation of the ENSO and GLB temperature curves is shown in Figure 6 reveals a very strong correlation covering the majority of the data within 95% confidence interval. The Pearson and Spearman correlation coefficients calculated in assumption of normal and multivariate data distribution are equal to 0.887 and 0.863, respectively, with a significance level of $P < 0.001$.

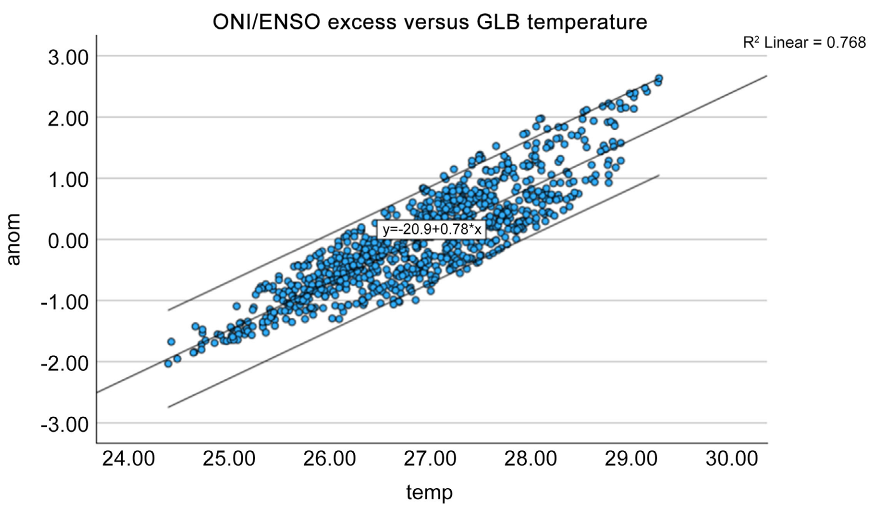

Figure 6. Scatter plot of the correlation of the excess of ONI/ENSO index versus the global land-ocean temperature ($r = 0.89$) approximated by linear fit (central line). The outer thin lines define the 95% confidence intervals, the χ^2 coefficients is equal to 0.768 as presented in the top right corner.

Previously, it was shown by [36] that the correlation coefficient between the averaged sunspot index and the ONI/ENSO index is close to zero (r = 0.01), and it is slightly better but still low (r = 0.10) for the correlation of the ENSO index with the solar magnetic cycle of 21.4 years, e.g. the summary curve of SBMF [23]. The ONI/ENSO was shown to have strong effects by Moon gravitation induced by oscillations of the lunar perigee, revolution of Jupiter on its orbit and orbital motion of Sun about the barycentre imposed by the gravitation of large planets [36], which provides a noticeable link of the ONI/ENSO index with the frequency of under-water volcanic eruptions, which frequencies, in turn, are affected by the solar magnetic cycle of 21.4 years [37].

3. SPECTRAL ANALYSIS OF TIME SERIES WITH A WAVELET TRANSFORM

In order to understand the nature of ongoing variations of different parameters of the terrestrial environment, such as variations of land-sea temperature, sea level, ONI/ENSO index and carbon dioxide abundances, let us explore their spectral properties using a wavelet analysis.

3.1. General Description of the Wavelet Transform Analysis

The series of the time-dependent data considered in the terrestrial environment are generated by complex processes, which are not fully known or understood. The most essential interests in such the systems are the ways to anticipate their appearances in the future. Most traditional mathematical methods investigating periodicities in a frequency domain, such as Fourier analysis, implicitly assume that the processes which form the temporal series are stationary in time that is not always the case.

While the wavelet transform allows to expand a temporal series into the frequency-time domain that allows to detect local patterns of a temporal series under investigation. Wavelet transform is a very useful instrument for the analysis of localised interruptive oscillations in the temporal series. The wavelet analysis is most beneficial for investigation of coupled time series which are somehow linked by natural processes forming them but not clearly known to the investigators. Even more beneficial for detecting these links is a cross-wavelet transform deriving the correlation and its relative phase in the time-frequency domain.

Continuous wavelet transform (CWT) of signals is the spectral analysis method providing a two-dimensional scan of the analysed signal (time and frequency, or period), in which the coordinates of the time and frequency are independent variables [38] as defined below

$$W_x(u,s)=\int_{-\infty}^{\infty} x(t)\frac{1}{\sqrt{s}}\Psi\left(\frac{t-u}{s}\right)\mathrm{d}t, \tag{1}$$

where u is temporal position, s is scale (inverse to frequency), and $\Psi=\Psi^M$ is Morlet wavelet defined as follows:

$$\Psi^M(t)=\left(\pi^{-\frac{1}{4}}\right)\mathrm{e}^{i\omega_0 t}\cdot\mathrm{e}^{-\frac{t^2}{2}}, \tag{2}$$

where $\omega_0=6$ for most geophysical applications [39].

This representation allows one to explore the properties of the signal simultaneously in time and frequency domains. This makes the wavelet analysis an excellent tool for examining the series with time-varying frequency characteristics [38]. By considering the time series in the frequency-time space it is possible to derive dominant periods and their variations in time. The mother wavelet was selected as the Morlet wavelet (the real part of it is damped function of cosine), because with this choice one can obtain a high frequency resolution, which is important for our task.

The power of the wavelet spectra is shown in plots with wavelets by a colour bar plotted next to the wavelet spectrum. The Cone of Influence (COI) [38] marked in the wavelet spectrum by the black dashed line, defines the parts of the spectrum with the essential border effects in the starting and finishing parts of the time series, because of a limited statistical data (boarder effects). Consequently, the results outside the COI are excluded from the further investigation [38]. This is particularly valid in the calculations of the global wavelet spectrum shown by the black curves on the right hand side from the wavelet spectra where the solid black lines represent the global wavelet spectra integrated over time. The black dashed lines in the global wavelet plots defines a 95% confidence interval for the global wavelet spectrum.

3.2. Cross-Wavelet Transform and Wavelet Coherence

One of the main advantages of using the Morley wavelet transform is the function of a wavelet coherence. Wavelet coherence is built on the continuous wavelet transform (CWT), which projects a time series $x(t)$ onto a set of time- and scale-localised basis functions (wavelets). Usually, the coherence function is used in practical application for establishing a reliable link of the processes in the frequency domain by allowing to establish a correlation of two time series in the domain of time-frequency.

Assuming there are two time series $x(t)$ and $y(t)$, their cross-wavelet transform can be defined as:

$$W_{xy}(u,s) = W_x(u,s) W_y^*(u,s). \tag{3}$$

from which the squared wavelet coherence is defined as follows:

$$R^2(u,s) = \frac{\left|S\left(s^{-1}W_{xy}(u,s)\right)\right|^2}{\left|S\left(s^{-1}W_x(u,s)\right)\right|^2 \left|S\left(s^{-1} | W_y(u,s)\right)\right|^2}, \tag{4}$$

where S is a smoothing operator in both time and scale that prevents from overfitting to a transient noise. The coherent function R^2 is ranging from 0 (no local correlation) to 1 (perfect local correlation).

Phase shift information is available through the argument of the smoothed cross-spectrum using its imaginary $\Im$ and real $\Re$ parts as follows:

$$\Delta\phi_{xy}(u,s) = \tan^{-1}\left(\frac{\Im\left[S\left(s^{-1}W_{xy}(u,s)\right)\right]}{\Re\left[S\left(s^{-1}W_{xy}(u,s)\right)\right]}\right), \tag{5}$$

which quantifies in-phase or anti-phase behaviour and a possible lead lag relationship.

Then the time lag $\Delta t(x,t)$ is calculated via the phase shift $\Delta\phi_{xy}$ as described below:

$$\Delta t(x,t) = \frac{\Delta\phi_{xy}(s,t)}{2\pi \cdot f(s)}, \tag{6}$$

where $f(s)$ is a frequency corresponding to the scale s, $\Delta\phi_{xy}$ is the phase angle in radians.

When the two series are in phase, the arrows are inclined to the right, e.g. the phase shift is positive, it means the series move in the same direction. While when the arrows are inclined to the left, or phase shift is negative, the series are in anti-phase meaning they move in the opposite directions [40]. The angles of inclination of the arrows on the wavelet coherence plot would indicate the phase relationship between the series, either one moving forward or lagging another. Hence, the phase angle shift $\Delta\phi$, which is linked to the time lag Δt from Equation (6) above, is indicated by the arrow inclination in wavelet coherence spectrum. The arrows are inclined to the right if the phase shifts are positive, e.g. the series 1 (CO_2 abundances) lag the series 2 (temperature) and the arrows are inclined to the left if the phase shifts are negative e.g. series 2 variations lag the series 1.

4. RESULTS OF SPECTRAL ANALYSIS OF CARBON DIOXIDE IN COMPARISON WITH OTHER TERRESTRIAL DATASETS

4.1. Spectral Variations of total CO_2 Abundances by Different Stations

The global spectral characteristics of CO_2 variations are found to be rather similar with that in MLO revealing the well defined (above 95% confidence level) periods of oscillations of 9 and 21.4 years and the period of 3.79 years occurring just within the 95% confidence level as shown in **Figure 7** in the global wavelet spectra depicted on the right side of the wavelet images.

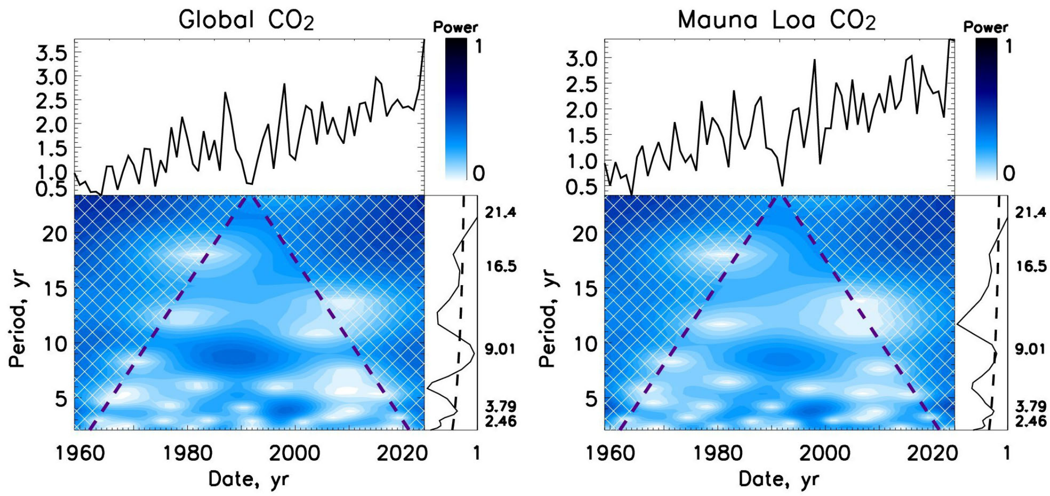

Figure 7. The wavelet analysis of the variations of the global (left) and MLO (right) CO_2 abundances. The CO_2 global and MLO variations are plotted in the top left sides of each image with their wavelet spectra shown in the bottom left sides of each image with the black dashed lines showing the Cone of Influence (COI) [38]. The wavelet spectral powers are marked by the colour bars in each image (the top right plots) and the global wavelet spectra (black solid line) integrated over times are shown in the bottom right plots with the black dashed lines indicating the 95% confidence intervals of the detected spectral features.

The period of 21.4 years derived in the wavelet spectra for global and MLO variations of CO_2 is clearly linked to the variations of the solar activity expressed through the summary curve of the two eigen vectors of the solar background magnetic field [23], which has a double period of the solar activity cycle of 10.7 years defined by the sunspot numbers [41]. Evidently, the maximum CO_2 abundance is produced during the solar cycles with a dominant southern magnetic polarity occurring in the even cycles, which, in turn, are producing maximal geomagnetic effects on the terrestrial magnetosphere and atmosphere.

The oscillation periods of 9 and 3.79 years have less certain links with the solar activity as such, but might be linked to the combined effects of some other factors of the terrestrial environment like global mean sea level (GMSL) and El Nino Southern Oscillations (ENSO). These, in turn, were found to be affected by the gravitation of Jupiter on the Sun and Earth inducing ENSO oscillations via the increase of underwater volcanic eruptions and by the Moon passing its lunar perigee, thus, inducing small-scale oscillations of ENSO [36]. These points will be discussed in sections below.

4.2. Spectral Analysis of Carbon Dioxide in Comparison with Other Terrestrial Datasets

4.2.1. Comparison of CO_2 and Sea Level Variations

Let us first compare the datasets of the MLO CO_2 abundances with the variations of global sea level taken from the GMSL dataset as shown in **Figure 8**. It can be noted that there is a general trend of the increasing in time measurements of CO_2 and GMLS sea level (**Figure 8**, left plot). Although, the increase of CO_2 abundances appears to occur faster than the increase of the sea level.

This is reflected in the correlation coefficient r = 0.60 between these two datasets as demonstrated by the scatter plot in **Figure 8**, right plot. The scatter plot also shows a better fit by quadratic curve indicating a trend of mild saturation of the sea level effect in the production of CO_2. This indicates that despite the ocean-air exchange is rather intense and important for producing CO_2 presence in the air there are some other mechanisms affecting the CO_2 abundances, which grow faster than the increase of the sea level and temperature.

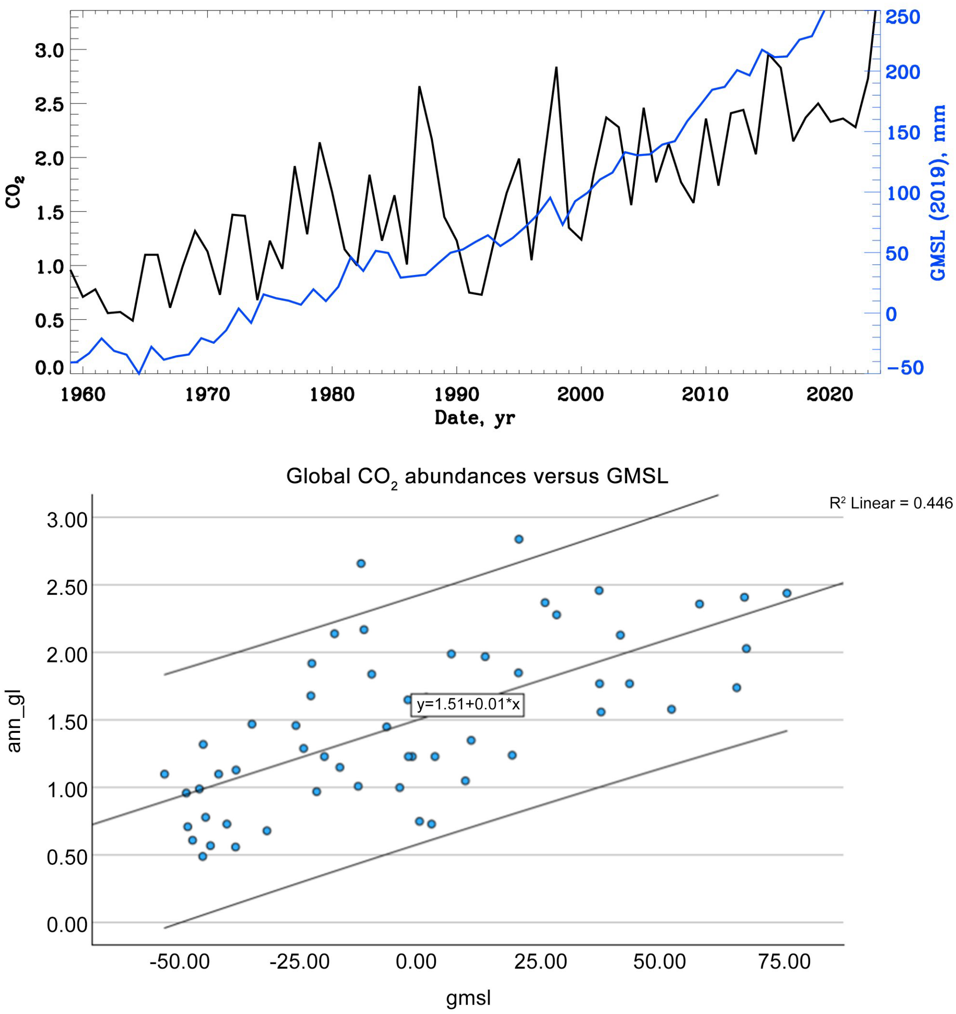

Figure 8. Top plot: comparison of variations of the MLO CO_2 abundances (black curve) versus the Global Mean Sea Level (GMSL) variations (blue curve). Bottom plot: the scatter plot of the correlation (r = 0.60) of the MLO CO_2 abundances versus the Global Mean Sea Level (GMSL) variations. The central black line shows a linear fit, wider black lines show the 95% confidence level of the data covered by the linear fit.

In order to gain more information about the changes let us run a spectral wavelet analysis of the GMSL datasets (2015 and 2019) shown in **Figure 9** and compare these with the wavelet spectrum obtained for the global and MLO CO_2 abundances shown in **Figure 7**. It can be observed from the global wavelet spectra in the right bottom plots in both CO_2 datasets (global and MLO) that there is a dominant (well above 95% confidence level) 21.4-year period of the variations for CO_2 datasets, as it was shown for CO_2 in section 4.1 and for the sea level GMSL with a period on 19.6 years shown in the wavelet spectra of the both GMSL dataset shown in **Figure 9**.

The similar period of 21.4 years corresponds exactly to the period of solar magnetic activity variations shown in the summary curve of the eigen vectors of solar background magnetic field [23, 41]. This double magnetic activity period of 21.4 years in CO_2 abundance variations indicates the undeniable natural effect of the Sun and solar radiation on the generation of carbon dioxide in the terrestrial atmosphere. This means any other (like anthropogenic) contributions to the CO_2 abundances are significantly lower than the natural ones that confirms the previous similar conclusions claiming only 5.5% contribution by fossil fuels [6, 7].

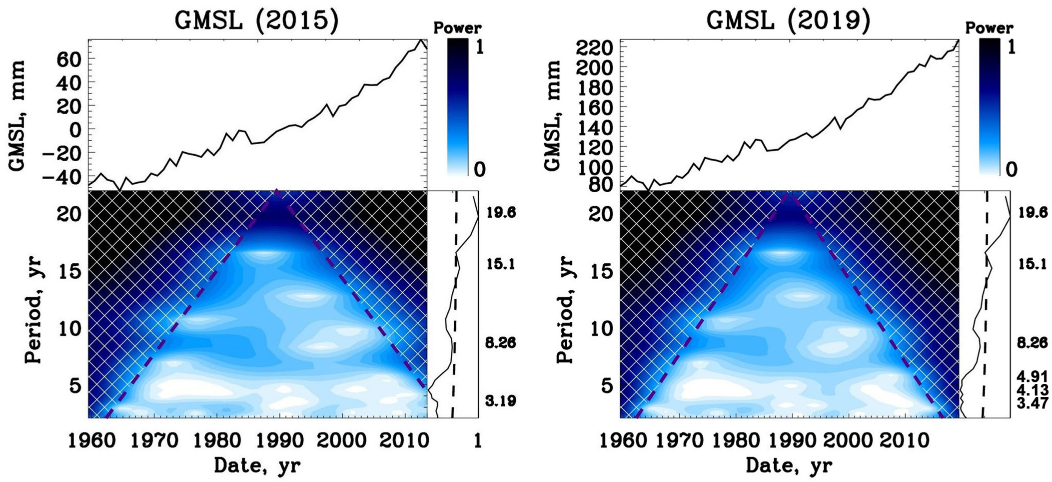

Figure 9. Wavelet spectra of the Global Mean Sea Level (GMSL) taken in 2015 (left image) and in 2019 (right image) datasets (see the text for more details). The GMSL temporal variations are plotted in the top left sides of each image with their wavelet spectra shown in the bottom left sides with the black dashed lines showing the Cone of Influence (COI). The wavelet spectral powers are marked by the colour bars in each image (the top right plots) and the global wavelet spectra (black solid line) integrated over times are shown in the bottom right plots with the black dashed lines indicating the 95% confidence intervals of the detected spectral features.

In addition, there is the other period of CO_2 variations of about 9 years clearly observed above the 95% confidence level, which can be linked to the similar period of 8.26 years in GMSL spectrum marked just at the border of this confidence level. This period of 9 years indicates to a possible link between the CO_2 variations with sea level and temperature variations as well as with the other phenomenon like ONI/ENSO index, which is discussed in the next section.

4.2.2. Variations of the Total CO_2 Abundances versus ONI/ENSO Variations

Comparison of the temporal variations of CO_2 abundances and ONI/ENSO index is shown in Figure 10 (left plot) and the scatter plot of their correlation in Figure 10 (right plot). It demonstrates a pretty moderate correlation of r = 0.24 indicating the ONI/ENSO index as such does not strongly affect the global CO_2 abundance appearances.

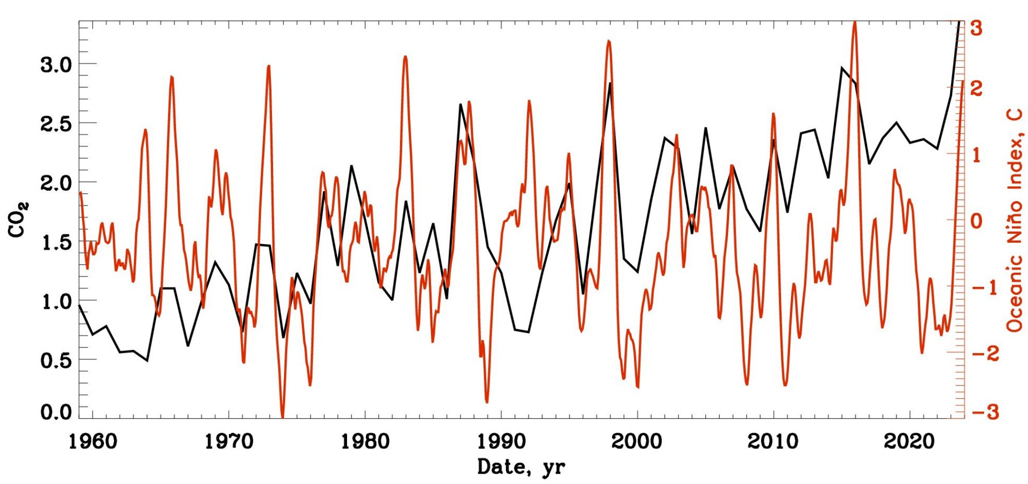

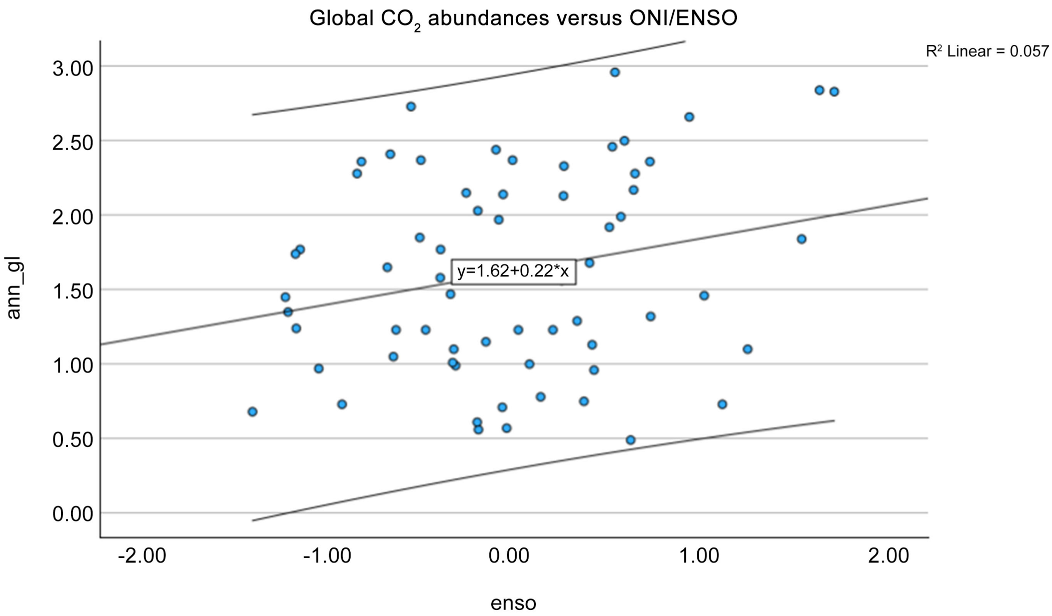

Figure 10. Top plot: variations of the global CO_2 abundances (black curve) versus ONI/ENSO index (red curve). Bottom plot: a scatter plot of the correlation (coefficient r = 0.24) of the global CO_2 and ONI/ENSO variations.

Although, a different story appears from a comparison of a de-trended plot of the global CO_2 abundances and ONI/ENSO variations shown in **Figure 11**, which show much stronger (r = 0.79) correlation. This indicates that CO_2 deviations from the averaged CO_2 abundances are significantly affected by the variations of ONI/ENSO index. Combined with the significant (r = 0.60) correlation of the global CO_2 with the sea level GMSL dataset this correlation indicates a significant role of exchange of CO_2 between the ocean and air based on Henry's law [42].

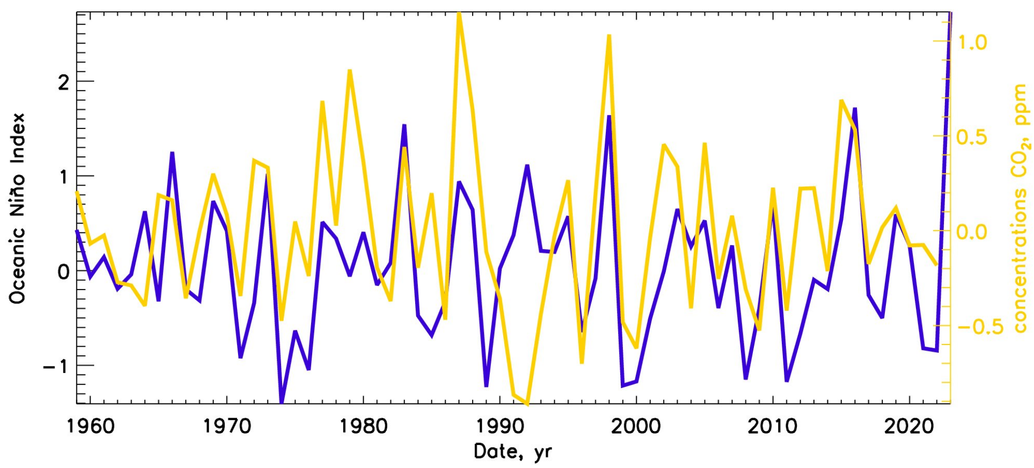

Figure 11. The variations of the de-trended (deviation from average) global CO_2 abundances (yellow curve) versus the ONI/ENSO index variations (purple curve) revealing the correlation coefficient r = 0.79.

Let us now apply the Morlet wavelet analysis to the CO_2 abundance and ONI/ENSO sets with the results presented in Figure 12. The most important feature derived from the ONI/ENSO index is a presence of the statistically significant periods of 3.57 - 5.05 and 12 years with some tendency to have a double 12-year period restricted by a short length of the ONI/ENSO data [36]. The lower period of 4 - 5 years in the ONI/ENSO index variations can be related to the effects of a half cycle of the lunar perigee oscillation of 8.85 years on the elliptical orbit of the Moon [36] leading to stronger tides twice a year when the lunar perigee is aligned with the Earth-Sun axis leading to the semidiurnal lunar tides [43]. This force can lead to the dominant positive Antarctic Oscillation (AAO) [11] and increase of volcanic eruptions [36].

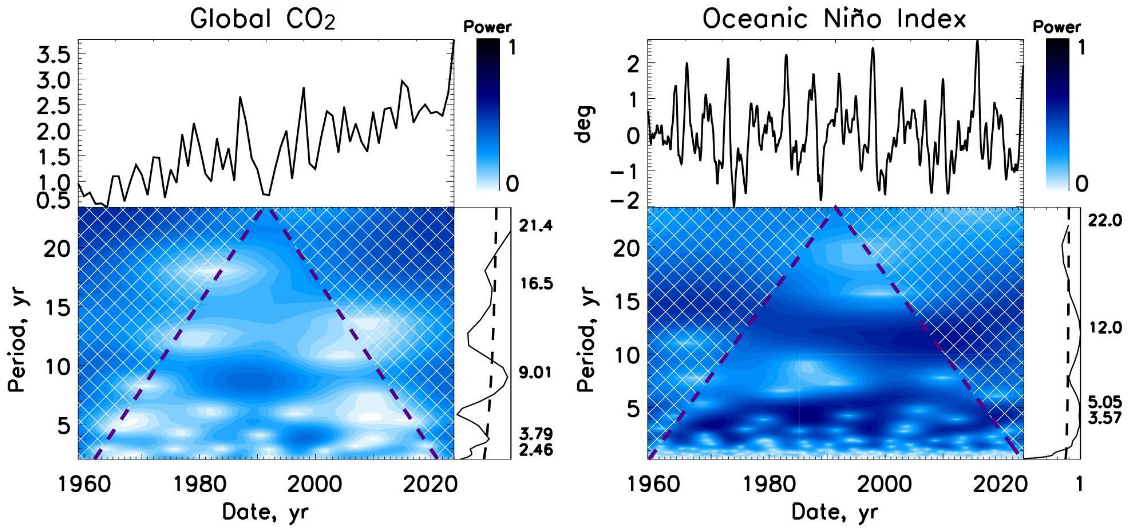

Figure 12. The wavelet analysis of the variations of the global CO_2 abundances (left image) and ONI/ENSO (right image). The CO_2 and ONI/ENSO temporal variations are plotted in the top left sides of each image with their wavelet spectra shown in the bottom left sides of each image. The wavelet spectral powers are marked by the colour bars in each image (the top right plots) and the global wavelet spectra (black solid line) integrated over times are shown in the bottom right plots with the black dashed lines indicating the 95% confidence intervals of the detected spectral features.

The larger period of 12 years in the ONI index, which is detected with the high accuracy within 95% confidence interval. This period is not linked to solar activity indices [36], which have the period of 10.7 years [41, 44]. Although, this 12-year period of the ONI/ENSO index oscillations is shown linked to the revolution of Jupiter and its gravitational effects on the Sun in it solar inertial motion [24]. These planetary effects on ONI/ENSO with periods of 4.5 - 5 and 12 years shown in Figure 12 combined with the correlation of the de-trended CO_2 abundance with ONI/ENSO variations (Figure 11) can help to understand the unusual period of 9 years in CO_2 variations which is likely to indicate the joint effect of the planetary influences of 12 (Jupiter) and 5 (Lunar perigee) years making the difference in the CO_2 abundances to reveal a maximum at the median period of 9 years.

4.2.3. Variations of CO_2 Abundances versus the GLB Temperature

The investigations of the links of CO_2 variations with the sea level and OBI/ENSO index variation brings us to a need to explore the link of CO_2 abundances to the terrestrial temperature variations which are compare directly with the GLB temperature in Figure 13 (left plot) and scatter plot of correlation shown the right plot. It shows a very close (82%) correlation of the CO_2 abundance s with the GLB temperature variation with the linear fit covering most of the data within 95% confidence level. It could be argued that the parabolic fit between the two datasets is aligned better with the data than a linear one.

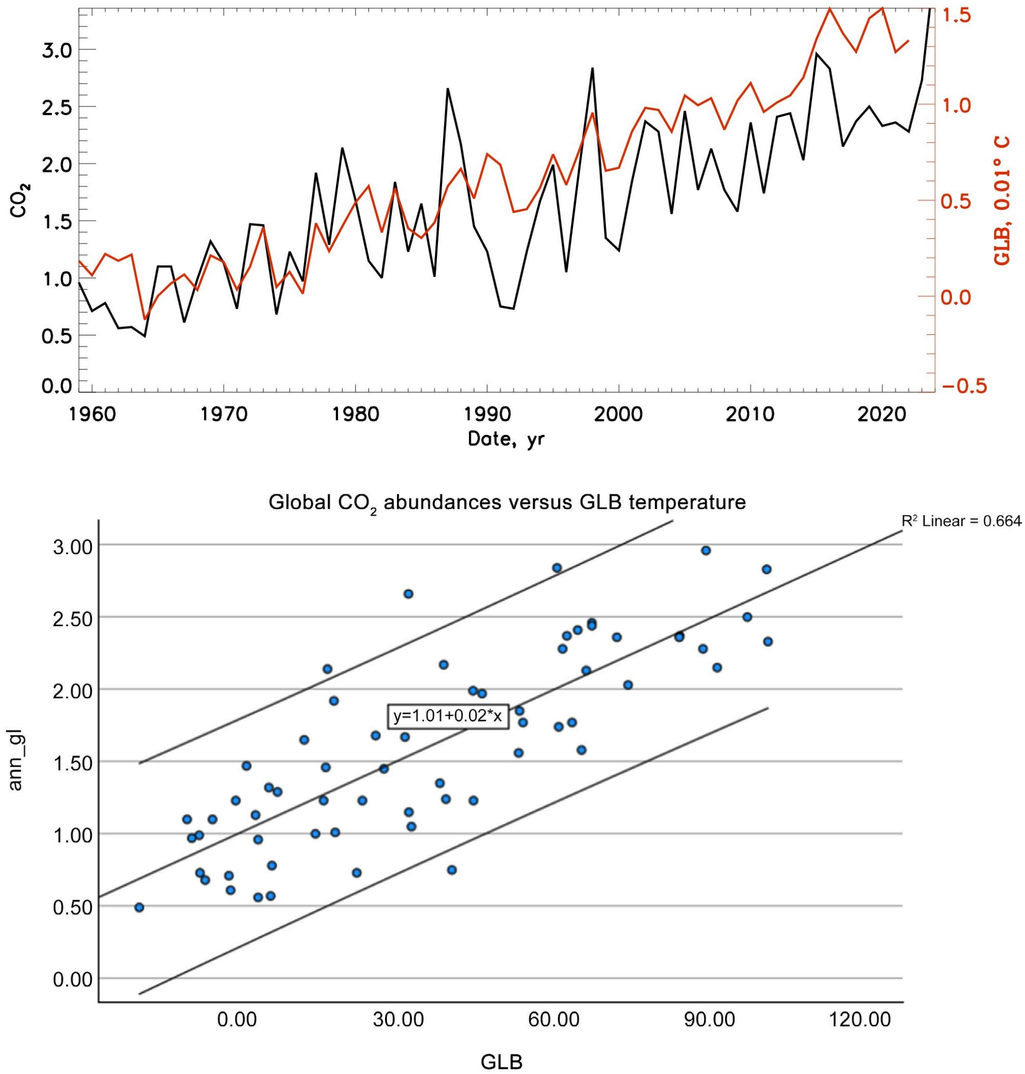

Figure 13. Top plot: tvariations of the global CO_2 abundances (black curve) versus the GLB terrestrial temperature (red curve). Bottom plot: scatter plot of the correlation (r = 0.82) of the global CO_2 abundances versus the global GLB) temperature variations. The red line presents linear fit of CO_2 and temperature, the central thin black line shows quadratic fit. The two thin black lines show the 95% confidence level of the data covered by the fits.

In order to evaluate the spectral properties of the series and to derive the key periods let us apply the Morlet wavelet analysis to the GLB temperature with the results presented in **Figure 14**. The most important feature derived from the GLB series of terrestrial temperature is a presence of the statistically significant periods of 21.4 years, similar to the variations of CO_2 and GMSL sea level. The period of 21.4 years which is the same as the oscillation period of a solar magnetic activity cycle (double sunspot cycle) derived in the summary curve of eigen vectors of the SBMF [41, 44]. There is some indication in the GLB temperature variations to a period of 8.26 years that can be related to the period of 9 years found in CO_2 variations.

Although this close correlation of two datasets (CO_2 and GLB) does not indicate clearly, which of the datasets is leading and which is lagging. This point can be explored with the cross-correlation and wavelet coherence discussed in the next section.

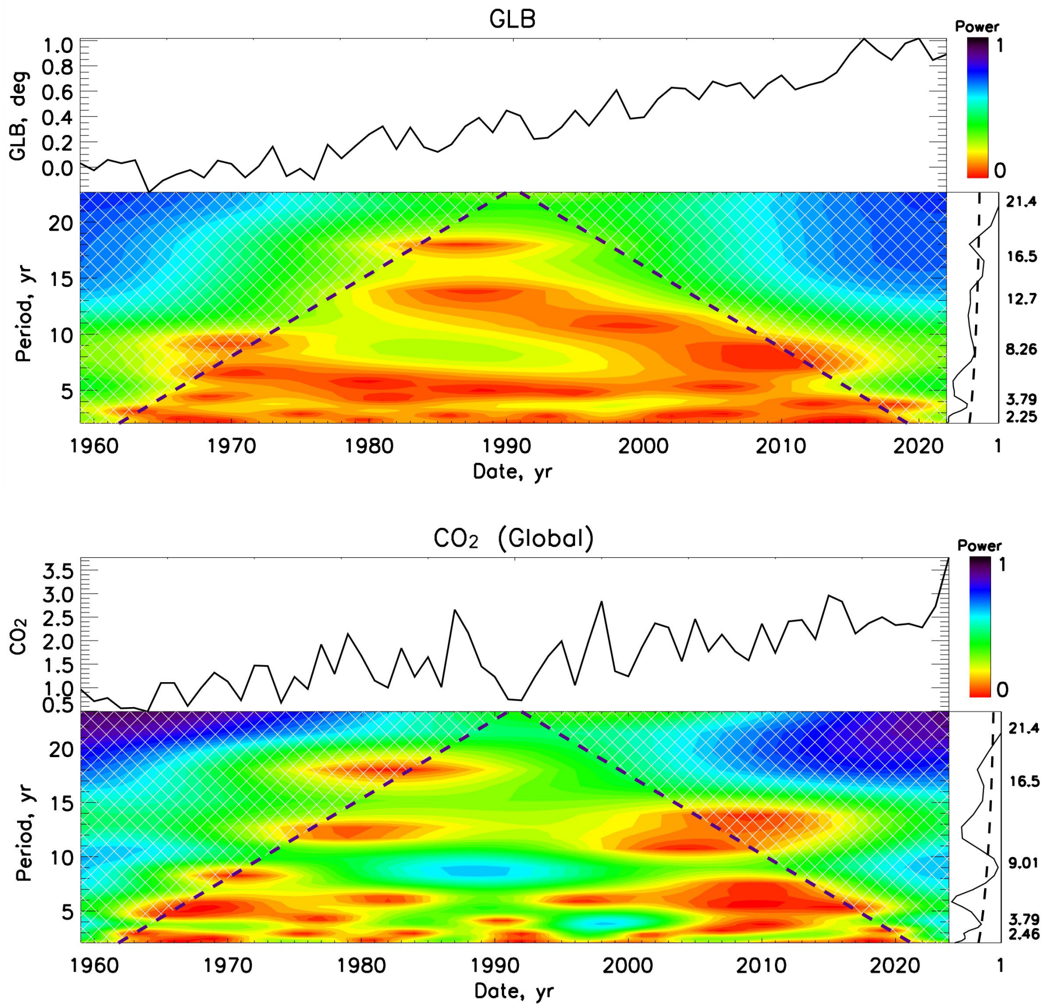

Figure 14. The wavelet analysis of the variations of the global GLB temperature (top image) and the global CO_2 abundances (bottom image). The GLB temperature and CO_2 variations are plotted in the top left sides of each image with their wavelet spectra shown in the bottom left sides of each image. The wavelet spectral powers are marked by the colour bars in each image (the top right plots) and the global wavelet spectra (black solid line) integrated over times are shown in the bottom right plots with the black dashed lines indicating the 95% confidence intervals of the detected spectral features.

4.3. Cross-Correlation and Wavelet Coherences of CO_2 Abundances and GLB Temperature

Lets first calculate the traditional cross-correlation of the series of CO_2 abundances and GLB temperatures presented In Figure 15 (top plot). The cross-correlation function clearly reveals the lag by CO_2 abundance of about 1 year from the GLB temperature variations that resembles the similar lag of CO_2 variations reported earlier by [6].

To enhance this finding let us now apply the coherence function of the cross-wavelet transform of the series of the CO_2 abundances and the GLB terrestrial temperature with the wavelet coherence spectrum shown in Figure 15 (bottom plot). The darker parts of the wavelet coherence spectrum correspond to a higher correlation (90% or higher) of the CO_2 and GLB temperature series while the lighter parts denote a weak correlation. The arrows indicate the phase shifts between the two series under the investigation for the intervals where the cross-correlation is higher than 0.9.

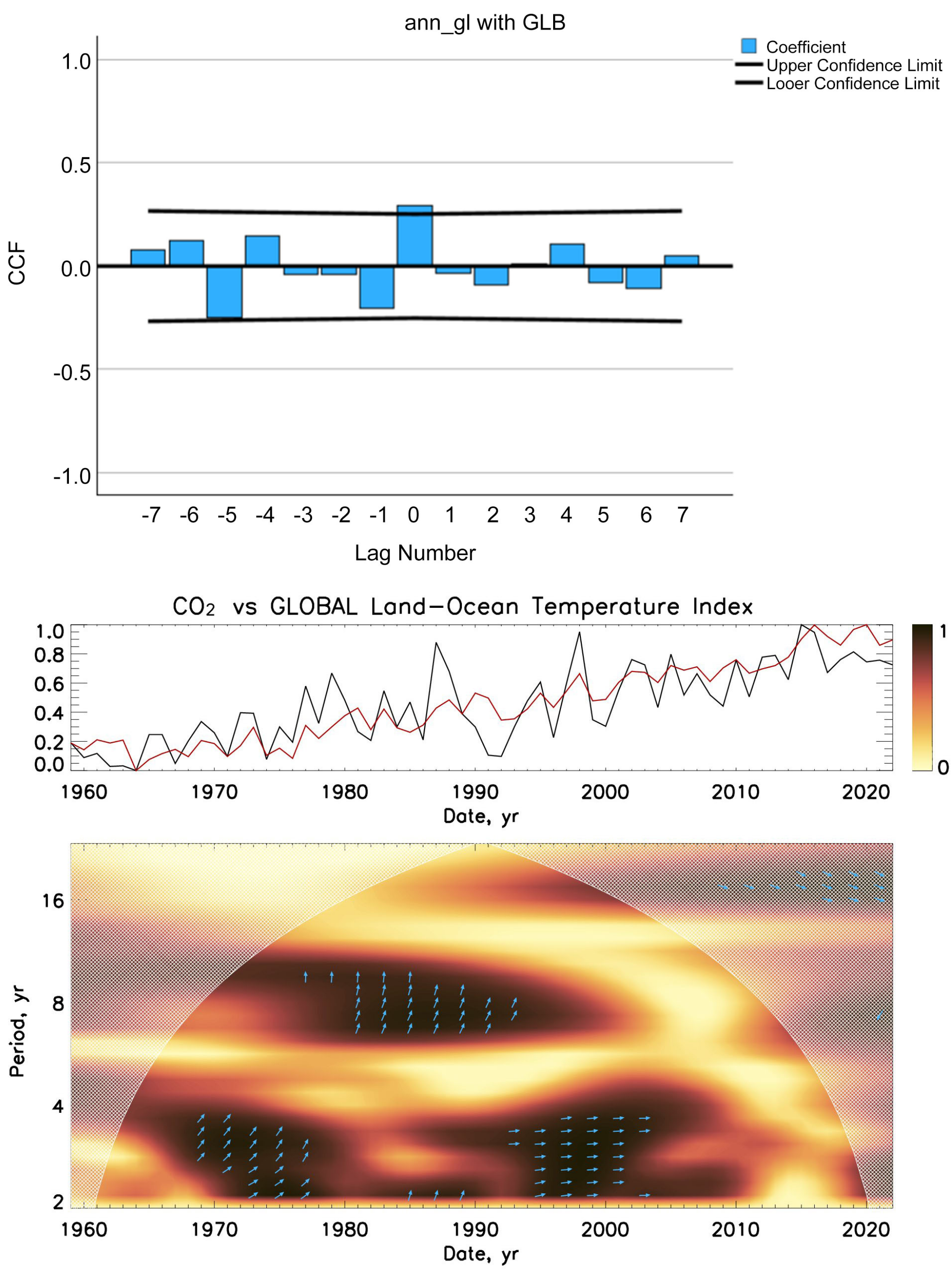

Figure 15. Top plot: cross-correlation of the global CO_2 variation and GLB temperature showing the time lag of CO_2 at least one year from GLB temperature. Bottom plot: the wavelet cross-correlation and coherence function showing a lag of CO_2 abundances from the GLB temperature by 1.2 - 1.8 years (see details in the text).

The arrow inclination to right (or left) indicates the series to be in phase (or anti-phase). A zero difference would indicate the series move coherently, the arrow inclination towards right indicate that the series of the CO_2 abundance lags the GLB temperature series. Hence, the arrows on the wavelet coherence plot indicate the phase relationship between the series, either moving forward or lagging. The angle of arrow inclination indicates the phase shift $\Delta\phi$ which can be linked to the time lag Δt as described in section 3.2.

We use the phase angle shift $\Delta\phi$ (Equation (5)) obtained on the 8 years scale for the strongest correlation of 0.9 shown in **Figure 15** (bottom plot) for the two series of CO_2 and GLB temperature variations and convert it into the time lag Δt using formula (Equation (6)). The positive Δt indicates there is a time lag (delay) of the CO_2 abundance variations with respect to the terrestrial GLB temperature series.

This coherence wavelet analysis revealing the strongest correlation (r > 0.9) of these two datasets allowed us to obtain a time difference for variations of CO_2 abundances and the GLB temperature to be equal to 1.2 - 1.8 years in the periods of >4 (1970-1975) or >8 (1980-1990) years. There was a coherence between these two datasets in 1995-2005 when the arrows become parallel to the X-axis as derived with wavelet coherence analysis in **Figure 15** (bottom plot). This indicates the two datasets, CO_2 and temperature can occasionally appear coherently with a period of 4 years while CO_2 abundances definitely lag the temperature variations with a period of 8 years.

This lag size of 1.2 - 1.8 years between the variations of CO_2 abundance and terrestrial temperature for a period of 8 years confirms more accurately the time lag of one year detected for the whole datasets using the cross-correlation function shown in **Figure 15** (top plot). This indicates that the CO_2 abundances follows the variations of terrestrial GLB temperature and not define them. Hence, carbon dioxide cannot be the force, which induces the temperature variations. The most likely force imposing the terrestrial temperature variation was suggested to have the links to solar radiation emitted either owing to solar magnetic activity with a period of 21.4 years or modulated by the orbital motion of the Sun and planets via their links with ONI/ENSO index.

5. DISCUSSION AND CONCLUSIONS

In this study we investigate global measurements of the total CO_2 abundances recorded at the US Samoa and Mauna Loa observatories as well as the global CO_2 variations produced from all the sets CO_2 observations at NOAA. The global CO_2 abundance variations were compared directly with variations of the global mean sea level (GMSL), ONI/ENSO variations and the global (GLB) terrestrial temperature. Annual variations of the CO_2 abundances in time are shown to have the best fit by a parabolic curve with concavity up while the linear fit has shown systematic deviations indicating a parabolic curvature of the observed curve.

Hence, the measurements of the total (global) annually averaged CO_2 variations, which by default should contain both natural and anthropogenic CO_2 parts in the measured data, do not reveal any noticeable signs of the latter because of a lack of similarity of the measured curve to the linear CO_2 curve assigned to the one produced from the fossil fuel usage. This conclusion is also confirmed by a lack of increase of the isotope ^{13}C contribution, usually associated with fossil fuels, in the CO_2 abundance measured in the past 40 years [8].

Although, there is a good correlation (r = 0.60) between CO_2 abundances variations and the sea level GMSL datasets and much stronger correlation (0.82) of CO_2 variations and the GLB terrestrial temperature. The link of CO_2 variations to the ONI/ENSO index is not very strongly correlated (r = 0.24), while the with the ONI/ENSO index is shown to have stronger correlation (r = 0.79) with the de-trended variations of CO_2 above the averaged level is highly that indicates to a complex effect of the CO_2 exchange between sea and air governed by ONI/ENSO.

Spectral analysis with Morlet wavelet transform allows us to derive the wavelet spectra of global and MLO CO_2 variations to have well-defined (above 95% confidence level) periods of oscillation of 21.4 and 9 years and the period of 3.79 years occurring within the 95% confidence level. Moreover, the wavelet analysis allowed to uncover the key periods of the variations of CO_2 (21.4, 9 and 3.7 years), GMSL (21.4, 8.5 years), ENSO (21.4, 12 and 4.5 years) and terrestrial temperature (21.4, 8.36 and 3.75 years).

The presence of a common period of 21.4 years in all the datasets of temperature and global sea level including also CO_2 abundances indicates that these datasets are all affected by the same natural source, namely, by the cyclic variations of solar background magnetic field in double cycle of solar activity [23]. The CO_2 abundance oscillations with a period of 9 years can be linked to the variations ONI/ENSO with periods of 4.5 and 12 years. This link is combined with the correlation of the de-trended CO_2 abundance with

ONI/ENSO variations, which can explain how the ONI/ENSO index modulates the observed CO_2 variations. This period is likely to indicate the joint effect of the planetary influences on the ONI/ENSO index which is shown affected by 12-year period of Jupiter revolution and 4.5 - 5 years variations of Lunar perigee, which jointly make the maximum difference in the CO_2 abundances at the median period of 9 years.

Thus, the natural periods of CO_2 abundance oscillations linked to the similar periods in GMSL and ONI/ENSO indices indicate that the production of CO_2 on Earth is mainly governed by natural processes of the air-ocean exchanges modulated by the variations of solar background magnetic field and solar activity.

The most important correlation ($r = 0.89$) is found between the variations of the global CO_2 abundances and GLB terrestrial temperature indicating a strong relationship between these two entities. The cross-correlation analysis allowed us to establish the time lag of one year for the CO_2 abundance from the GLB temperature variations, which was preciously reported by other researchers [6]. Furthermore, the coherence wavelet analysis of the global CO_2 and GLB terrestrial temperature variations established their strong correlation ($r > 0.9$) and derived that CO_2 abundance variations lags the temperature variations by 1.2 - 1.8 years during the most intervals of the CO_2 observations.

From the present analysis it becomes clear that the main variations of the carbon dioxide abundances should have natural causes linked to the solar activity, exchange of CO_2 between the air and ocean and some other gravitational effects via ONI/ENSO variations. If there are any additions to the current CO_2 abundances by the anthropogenic use of the carbon dioxide in fossil fuel, these additions are not revealed from the global CO_2 observations meaning they must be much smaller than the natural effects of the terrestrial environment imposed by the solar activity, solar magnetic field and the ONI/ENSO index variations.

DATA AVAILABILITY

The freely available datasets used in this study are listed below.

1) NOAA's General Monitoring Laboratory (GML) CO_2 datasets [17-19]. This dataset was produced by NOAA and is not subject to copyright protection in the United States. NOAA waives any potential copyright and related rights in these data worldwide through the Creative Commons Zero v1.0 Universal Public Domain Dedication (CC0 1.0) [19].

a) Globally averaged marine surface CO_2 annual mean data [19]:
https://gml.noaa.gov/ccgg/trends/gl_data.html;
https://gml.noaa.gov/webdata/ccgg/trends/co2/co2_annmean_gl.txt.

b) Globally averaged marine surface annual mean CO_2 growth rates [19]:
https://gml.noaa.gov/ccgg/trends/data.html; https://gml.noaa.gov/webdata/ccgg/trends/co2/co2_gr_gl.txt.

Other NOAA GML CO_2 datasets [19]:

a) Mauna Loa CO_2 annual mean growth rates [1, 17]:
https://gml.noaa.gov/webdata/ccgg/trends/co2/co2_gr_mlo.txt.

b) Mauna Loa CO_2 annual mean data [1, 17]:
https://gml.noaa.gov/webdata/ccgg/trends/co2/co2_annmean_mlo.txt.

c) Samoa Observatory data [19]: https://gml.noaa.gov/data/dataset.php?item=smo-co2-flask-month

This dataset was produced by NOAA and is not subject to copyright protection in the United States. NOAA waives any potential copyright and related rights in these data worldwide through the Creative Commons Zero v1.0 Universal Public Domain Dedication (CC0 1.0) [19].

2) The Global Mean Sea Level (GMSL) datasets:

a) GMSL dataset obtained during 1880-2014 (named GMSL(2015)) was obtained from the Centre for Protection of the Environment of the USA and SCIRO (Centre for Scientific and Industrial Research Organisation)
http://data-cbr.csiro.au/thredds/catalog/catch_all/OA_SLE_processed/Sea_Level_data/gmsl_files/catalog.html accessed on 29/07/2023 [22].

b) The same GMSL dataset extended to 2019 (named GMSL(2019)) was accessed on 25/05/2025,
http://data-cbr.csiro.au/thredds/catalog/catch_all/OA_SLE_processed/Sea_Level_data/gmsl_files/catalog.html.

3) Terrestrial temperature datasets:

a) HadCRUT5—the British Meteorological Center in Hadley and the department of Climate Research of the East Anglia University https://www.metoffice.gov.uk/hadobs/hadcrut5/, accessed on 12/06/2023 [20].

b) GLB: the surface temperature (GISSTEMP) produced by the NASA Goddard Institute of Space Science (GISS) https://data.giss.nasa.gov/gistemp/tabledata_v4/GLB.Ts+dSST.txt accessed 12/06/2023; https://data.giss.nasa.gov/gistemp/tabledata_v4/GLB.Ts+dSST.txt [21].

4) The Oceanic Niño Index (ONI) which also called as El Nina Southern Oscillation (ENSO), e.g. the Niño 3.4 index available since 1854 is taken from https://www.climate.gov/news-features/understanding-climate/climate-variability-oceanic-nino-index [35].

Software used for analysis:

1) Wavelet analysis software in IDL was provided by [38], available at http://paos.colorado.edu/research/wavelets/.

2) IBM SPSS Statistics v30.0 https://www.ibm.com/products/spss-statistics/gradpack is a comprehensive statistical analysis platform designed to help organisations and individuals extract reliable insights from data. It combines robust statistical testing, predictive modelling, regression, and forecasting with streamlined data preparation and automated analysis. With integrated AI capabilities, including the AI Output Assistant, users can interact with results using natural language—making complex outputs easier to understand and act on.

Authorised user licence is required and updated every year https://www.ibm.com/products/spss-statistics?utm_content=SRCWW&p1=Searchp&4=299294893835&p5=e&p9=171934014643&gclsrc=aw.ds&gad_source=1&gad_campaignid=22037412442&gbraid=0AAAAA-h2TOF3_WUtiv6WG-ci1rXhdeU3X&gclid=EAIaIQobChMIu5vOkOCilAMVe5JQBh1XhikpEAAYASAAEgKWrfD_BwE.

ACKNOWLEDGEMENTS

The authors wish to express many thanks for the data provided by the NOAA's Global Monitoring Laboratory (GML), which measures the abundances of carbon dioxide and other greenhouse gasses. We also appreciate the NASA Goddard Institute of Space Science (GISS) (US) and the British meteorological Center in Hadley, for providing the temperature datasets, the Centre for protection of the environment of the USA and the Centre for Scientific and Industrial Research Organisation for providing the data of the sea level and ONI/ENSO.

AUTHOR CONTRIBUTIONS STATEMENT

V.Z. formulated the problem, suggested the datasets to consider, did calculations and statistical analysis of the datasets with SPSS provided by IBM. I.V. gathered and processed the temperature, sea level data and ONI/ENSO index, analysed them with the wavelet tool, plotted the graphs. V.Z. and I.V. compared and analysed the results, wrote and reviewed the manuscript.

CONFLICTS OF INTEREST

The authors do not have any competing financial interests.

REFERENCES

1. Keeling, C.D., Bacastow, R.B., Bainbridge, A.E., Ekdahl, C.A., Guenther, P.R., Waterman, L.S., *et al.* (1976) Atmospheric Carbon Dioxide Variations at Mauna Loa Observatory, Hawaii. *Tellus A*: *Dynamic Meteorology and Oceanography*, **28**, 538-551. https://doi.org/10.3402/tellusa.v28i6.11322

2. Jaworowski, Z., Segalstad, T.V. and Ono, N. (1992) Do Glaciers Tell a True Atmospheric CO_2 Story? *Science of the Total Environment*, **114**, 227-284. https://doi.org/10.1016/0048-9697(92)90428-u

3. Trenberth, K.E. and Fasullo, J.T. (2009) Global Warming Due to Increasing Absorbed Solar Radiation. *Geophysical Research Letters*, **36**, L07706. https://doi.org/10.1029/2009gl037527

4. Ahlbeck, J.R. (2009) On the Increased Rate of Atmospheric Carbon Dioxide Accumulation 1980-2008. *Energy & Environment*, **20**, 1149-1154. https://doi.org/10.1260/095830509789876772

5. Soares, P.C. (2010) Warming Power of CO_2 and H_2O: Correlations with Temperature Changes. *International Journal of Geosciences*, **1**, 102-112. https://doi.org/10.4236/ijg.2010.13014

6. Salby, D. and Harde, H. (2022) Theory of Increasing Greenhouse Gases. *Science of Climate Change*, **2**, 212-238.

7. Veyres, C., Maurin, J.C. and Poyet, P. (2025) Revisiting the Carbon Cycle. *Science of Climate Change*, **5**, 135-185.

8. Koutsoyiannis, D. (2024) Net Isotopic Signature of Atmospheric CO_2 Sources and Sinks: No Change since the Little Ice Age. *Sci*, **6**, Article 17. https://doi.org/10.3390/sci6010017

9. Gervais, F. (2016) Anthropogenic CO_2 Warming Challenged by 60-Year Cycle. *Earth-Science Reviews*, **155**, 129-135. https://doi.org/10.1016/j.earscirev.2016.02.005

10. Humlum, O., Stordahl, K. and Solheim, J. (2013) The Phase Relation between Atmospheric Carbon Dioxide and Global Temperature. *Global and Planetary Change*, **100**, 51-69. https://doi.org/10.1016/j.gloplacha.2012.08.008

11. Roy, I. (2018) Addressing on Abrupt Global Warming, Warming Trend Slowdown and Related Features in Recent Decades. *Frontiers in Earth Science*, **6**, Article 136. https://doi.org/10.3389/feart.2018.00136

12. Salby, M.L., Titova, E.A. and Deschamps, L. (2012) Changes of the Antarctic Ozone Hole: Controlling Mechanisms, Seasonal Predictability, and Evolution. *Journal of Geophysical Research*: *Atmospheres*, **117**, D10111. https://doi.org/10.1029/2011jd016285

13. Easterbrook, D.J. (2016) Evidence-Based Climate Science. Elsevier.

14. Ato, D. (2024) Multivariate Analysis Rejects the Theory of Human-Caused Atmospheric Carbon Dioxide Increase: The Sea Surface Temperature Rules. *Science of Climate Change*, **4**, 1-15.

15. Koutsoyiannis, D., Onof, C., Kundzewicz, Z.W. and Christofides, A. (2023) On Hens, Eggs, Temperatures and CO_2: Causal Links in Earth's Atmosphere. *Sci*, **5**, Article 35. https://doi.org/10.3390/sci5030035

16. IPCC (2025) AR7 Climate Change: Impacts, Adaptation and Vulnerability. The Physical Science Basis.

17. Thoning, K.W., Tans, P.P. and Komhyr, W.D. (1989) Atmospheric Carbon Dioxide at Mauna Loa Observatory: 2. Analysis of the NOAA GMCC Data, 1974-1985. *Journal of Geophysical Research*: *Atmospheres*, **94**, 8549-8565. https://doi.org/10.1029/jd094id06p08549

18. Conway, T.J., Tans, P.P., Waterman, L.S., Thoning, K.W., Kitzis, D.R., Masarie, K.A., *et al.* (1994) Evidence for Interannual Variability of the Carbon Cycle from the National Oceanic and Atmospheric Administration/Climate Monitoring and Diagnostics Laboratory Global Air Sampling Network. *Journal of Geophysical Research*: *Atmospheres*, **99**, 22831-22855. https://doi.org/10.1029/94jd01951

19. Lan, X., Tan, P. and Thoning, K.W. (2026) Trends in Atmospheric Carbon Dioxide. MDT. Publication Information/Link. https://gml.noaa.gov/ccgg/trends/global.html?doi=10.15138/9n0h-zh07

20. Morice, C.P., Kennedy, J.J., Rayner, N.A., Winn, J.P., Hogan, E., Killick, R.E., *et al.* (2021) An Updated Assessment of Near-Surface Temperature Change from 1850: The Hadcrut5 Data Set. *Journal of Geophysical Research*: *Atmospheres*, **126**, e2019JD032361. https://doi.org/10.1029/2019jd032361

21. Lenssen, N.J.L., Schmidt, G.A., Hansen, J.E., Menne, M.J., Persin, A., Ruedy, R., *et al.* (2019) Improvements in the GISTEMP Uncertainty Model. *Journal of Geophysical Research*: *Atmospheres*, **124**, 6307-6326. https://doi.org/10.1029/2018jd029522

22. Church, J.A. and White, N.J. (2011) Sea-Level Rise from the Late 19th to the Early 21st Century. *Surveys in Geophysics*, **32**, 585-602. https://doi.org/10.1007/978-94-007-2063-3_17

23. Zharkova, V.V., Shepherd, S.J., Popova, E. and Zharkov, S.I. (2015) Heartbeat of the Sun from Principal Component Analysis and Prediction of Solar Activity on a Millenium Timescale. *Scientific Reports*, **5**, Article No. 15689. https://doi.org/10.1038/srep15689

24. Zharkova, V.V. and Vasilieva, I. (2023) Terrestrial Temperature, Sea Levels and Ice Area Links with Solar Activity and Solar Orbital Motion. *Natural Science*, **15**, 233-255. https://doi.org/10.4236/ns.2023.159018

25. Church, J.A. and White, N.J. (2006) A 20th Century Acceleration in Global Sea-Level Rise. *Geophysical Research Letters*, **33**, L01602. https://doi.org/10.1029/2005gl024826

26. Cazenave, A. and Nerem, R.S. (2004) Present-Day Sea Level Change: Observations and Causes. *Reviews of Geophysics*, **42**, RG3001. https://doi.org/10.1029/2003rg000139

27. Leuliette, E.W., Nerem, R.S. and Mitchum, G.T. (2004) Calibration of Topex/Poseidon and Jason Altimeter Data to Construct a Continuous Record of Mean Sea Level Change. *Marine Geodesy*, **27**, 79-94. https://doi.org/10.1080/01490410490465193

28. Fox-Kemper, B., Hewitt, H.T., Xiao, C., Aethalgeirsdottir, G., Drijfhout, S.S., Edwards, T.L., *et al.* (2021) Ocean, Cryosphere and Sea Level Chang. Cambridge University Press.

29. Rahmstorf, S. (2007) A Semi-Empirical Approach to Projecting Future Sea-Level Rise. *Science*, **315**, 368-370. https://doi.org/10.1126/science.1135456

30. Nerem, R.S., Beckley, B.D., Fasullo, J.T., Hamlington, B.D., Masters, D. and Mitchum, G.T. (2018) Climate-Change-Driven Accelerated Sea-Level Rise Detected in the Altimeter Era. *Proceedings of the National Academy of Sciences of the United States of America* **115**, 2022-2025. https://doi.org/10.1073/pnas.1717312115

31. Storch, H.V., Zorita, E. and González-Rouco, J.F. (2008) Relationship between Global Mean Sea-Level and Global Mean Temperature in a Climate Simulation of the Past Millennium. *Ocean Dynamics*, **58**, 227-236. https://doi.org/10.1007/s10236-008-0142-9

32. Grinsted, A., Moore, J.C. and Jevrejeva, S. (2010) Reconstructing Sea Level from Paleo and Projected Temperatures 200 to 2100 Ad. *Climate Dynamics*, **34**, 461-472. https://doi.org/10.1007/s00382-008-0507-2

33. Vermeer, M. and Rahmstorf, S. (2009) Global Sea Level Linked to Global Temperature. *Proceedings of the National Academy of Sciences of the United States of America*, **106**, 21527-21532. https://doi.org/10.1073/pnas.0907765106

34. Sannino, G., Carillo, A., Iacono, R., Napolitano, E., Palma, M., Pisacane, G., *et al.* (2022) Modelling Present and Future Climate in the Mediterranean Sea: A Focus on Sea-Level Change. *Climate Dynamics*, **59**, 357-391. https://doi.org/10.1007/s00382-021-06132-w

35. Kaplan, A., Cane, M.A., Kushnir, Y., Clement, A.C., Blumenthal, M.B. and Rajagopalan, B. (1998) Analyses of Global Sea Surface Temperature 1856-1991. *Journal of Geophysical Research*: *Oceans*, **103**, 18567-18589. https://doi.org/10.1029/97jc01736

36. Zharkova, V.V. and Vasilieva, I. (2024) ENSO Index Variations and Links with Solar and Volcanic Activity. *Natural Science*, **16**, 25-44. https://doi.org/10.4236/ns.2024.164004

37. Vasilieva, I. and Zharkova, V. (2023) Terrestrial Volcanic Eruptions and Their Association with Solar Activity. arXiv: 2203.03637.

38. Torrence, C. and Compo, G.P. (1998) A Practical Guide to Wavelet Analysis. *Bulletin of the American Meteorological Society*, **79**, 61-78. https://doi.org/10.1175/1520-0477(1998)079<0061:apgtwa>2.0.co;2

39. Vacha, L. and Barunik, J. (2012) Co-Movement of Energy Commodities Revisited: Evidence from Wavelet Coherence Analysis. *Energy Economics*, **34**, 241-247. https://doi.org/10.1016/j.eneco.2011.10.007

40. Jevrejeva, S., Moore, J.C. and Grinsted, A. (2004) Oceanic and Atmospheric Transport of Multiyear El Niño-Southern Oscillation (ENSO) Signatures to the Polar Regions. *Geophysical Research Letters*, **31**, L24210.

https://doi.org/10.1029/2004gl020871

41. Zharkova, V.V., Vasilieva, I., Shepherd, S.J. and Popova, E. (2023) Periodicities in Solar Activity, Solar Radiation and Their Links with Terrestrial Environment. *Natural Science*, **15**, 111-147. https://doi.org/10.4236/ns.2023.153010

42. Henry, W. (1803) Experiments on the Quantity of Gases Absorbed by Water, at Different Temperatures, and under Different Pressures. *Philosophical Transactions of the Royal Society of London Series I*, **93**, 29-42, 274.

43. Haigh, I.D., Eliot, M. and Pattiaratchi, C. (2011) Global Influences of the 18.61 Year Nodal Cycle and 8.85 Year Cycle of Lunar Perigee on High Tidal Levels. *Journal of Geophysical Research*, **116**, C06025. https://doi.org/10.1029/2010jc006645

44. Zharkova, V.V., Vasilieva, I., Popova, E. and Shepherd, S.J. (2023) Comparison of Solar Activity Proxies: Eigenvectors versus Averaged Sunspot Numbers. *Monthly Notices of the Royal Astronomical Society*, **521**, 6247-6265. https://doi.org/10.1093/mnras/stad1001